Nuclear Materials and Energy 40 (2024) 101715

Contents lists available at ScienceDirect

Nuclear Materials and Energy

journal homepage: www.elsevier.com/locate/nme

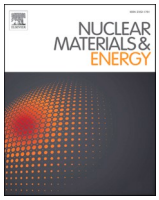

Structural integrity evaluation of the DTT plasma facing unit using detailed CFD and thermo-mechanical analyses

Patrik Tarfila [a,*], Oriol Costa Garrido [a], Boštjan Končar [a], Emanuela Martelli [b], Francesco Giorgetti [b,c], Selanna Roccella [b]

[a] Jožef Stefan Institute, Jamova Cesta 39, 1000 Ljubljana, Slovenia
[b] ENEA, Department of Fusion and Nuclear Safety Technology, 00044 Frascati, RM, Italy
[c] DTT S.c.a r.l., Via E. Fermi 45, I-00044, Frascati, RM, Italy

ARTICLE INFO

Keywords:
DTT
Divertor
Plasma facing unit
CFD
Tungsten monoblock
Structural integrity analysis

ABSTRACT

A new Divertor Tokamak Test (DTT) facility is currently being built in Italy to investigate different divertor configurations under different plasma scenarios. The divertor and in particular its target, consisting of Plasma Facing Units (PFUs), is exposed to high heat loads due to plasma fluence. In this paper, the structural integrity of the PFU is evaluated for a reference Single Null (SN) divertor configuration under three different plasma scenarios. A comprehensive structural integrity analysis has been carried out in three stages. In the first stage, computational fluid dynamic (CFD) analyses of the divertor's PFU with a cooling channel were performed at three different heat loads corresponding to three plasma scenarios. The temperature fields calculated by the CFD analyses were then used as input for the second stage, in which thermo-mechanical simulations were performed to predict the stresses and displacements in the PFU. Due to the high local heat loads, high stresses or even yielding are expected in the PFU's structural components. Therefore, in the third stage, the structural integrity of critical cross-sections has been verified using the Structural Design Criteria for In-vessel Components (SDC-IC). It has been demonstrated that structural components of the PFU are able to withstand the expected loads, although some non-structural components experienced yielding while not exceeding the critical values.

1. Introduction

The divertor is a component in fusion reactors that serves as an exhaust system for plasma impurities and is designed to handle extremely high heat fluxes. The heat fluxes on the divertor plasma-facing surfaces (targets) are very high, therefore the divertor targets, consisting of multiple Plasma-Facing Units (PFUs), need water-cooling to remove excess heat and have to be manufactured of appropriate structural materials [1].

The Divertor Tokamak Test (DTT) facility is being built in Frascati, Italy with the aim to test several divertor configurations under different plasma scenarios [1,2]. The DTT divertor target design is very similar to that in ITER and DEMO targets, which include tungsten monoblocks and a copper interlayer between the monoblocks and the cooling pipe made of CuCrZr [3–6]. The manufacturing process of DTT PFUs is described in [7]. Current experimental research efforts in High Heat Flux (HHF) facilities are focused on evaluating the endurance of the PFU mock-ups, subjected to cyclic loads under high heat fluxes up to 40 MW/m^2 [8–11]. In parallel to HHF experiments, modeling of temperature [4,8–13], stresses [11–13] and strains [10,12,13] is also necessary to predict the component response during normal operation and under plasma upset conditions. A recent study [14] has presented the thermo-mechanical simulations of the divertor PFU for the JT60SA tokamak device using electro-magnetic and plasma-heat loads, along with the structural integrity analysis utilizing linear-elastic material properties. These thermo-mechanical simulations used a fixed average fluid temperature and a heat transfer coefficient (HTC) for the pipes with swirl tape inserts, determined by empirical correlations. The empirical models for HTC are based on experimental results and are thus only valid in certain ranges of experimental conditions, fluid properties and geometries tested. They are developed on the basis of averaged flow properties and therefore cannot capture the local heat transfer behavior at the solid–fluid interface.

Preliminary calculations of the DTT divertor module design included computational fluid dynamics (CFD) analyses of hydraulic characteristics of the PFUs and cassette cooling channels [15], without considering

* Corresponding author.
E-mail address: patrik.tarfila@ijs.si (P. Tarfila).

https://doi.org/10.1016/j.nme.2024.101715
Received 29 February 2024; Received in revised form 22 July 2024; Accepted 23 July 2024
Available online 26 July 2024

heat loads. These analyses provided the first estimates of the overall pressure drop and mass flow rate distribution among the cooling pipes in the divertor module. Thermo-mechanical analyses of a small part of the PFU consisting only of a 90° elbow have also been performed in [16]. In this case, a heat transfer coefficient and a constant (bulk) fluid temperature with a heat load of 5 MW/m^2 were assumed. The temperature distributions and Mises stresses were presented by analyzing the integrity of 10 path locations within the elbow assuming linear-elastic material.

The next step in the divertor design requires analyses with more accurate predictions of the PFU's fluid thermo-hydraulic and thermo-mechanical responses considering realistic heat fluxes and mechanical boundaries between the PFUs and the cassette. Plasma physics simulations of different Single Null (SN) plasma scenarios [17] have provided the input heat flux distributions for the work presented here, and preliminary studies of the detached SN scenario have aided the development of the computational models [18,19]. The analyses in this paper thus follow a typical, yet comprehensive and thorough, methodology: from detailed CFD simulations to resolve the fluid behavior and temperature distribution in the structures, to thermo-mechanical simulations that use the structural temperatures as input loads to obtain displacements, strains and stresses. The final step is the structural integrity analysis following the Structural Design Criteria for In-vessel Components (SDC-IC) [20]. This methodology is applied to three heat loads, corresponding to three plasma scenarios.

To support the development and design of the DTT divertor, this study provides the results of a comprehensive structural integrity analysis of the divertor PFU, considering realistic thermo-mechanical loads and temperature distributions in the structures that are obtained by detailed computational simulations. The PFU design and heat loads are presented in Section 2, the CFD and thermo-mechanical analyses are presented respectively in Sections 3 and 4, the structural integrity analyses following the SDC-IC are described in Section 5 and the main conclusions are given in Section 6.

2. PFU design and heat loads

2.1. PFU design

A cross-section of the DTT fusion reactor with the divertor location (Fig. 1A), the divertor module and a single PFU are shown Fig. 1B and C respectively. The divertor module in Fig. 1B consists of a cassette and a total of 9 PFUs divided in three segments, namely the Inner Vertical Target (IVT), the Outer Vertical Target (OVT) and the flat central dome [16]. Seven out of 9 PFUs are such that a single water-cooled pipe connects and cools-down all three segments in series (see Fig. 1C). Two additional short PFUs with their own water-cooled pipes are added on each side of the OVT to accommodate the larger surface area of the OVT (Fig. 1B on the right).

The PFU geometry shown in Fig. 1C was prepared in ANSYS Workbench [21] and ABAQUS [22] for later use in subsequent analyses.

The PFU is based on the 'ITER-like' monoblock design. Its geometry incorporates six solid domains/components, as well as one fluid domain. These are shown in Fig. 2 and listed below together with the different materials of the PFU components:

- Monoblock (Tungsten – W)
- Copper interlayer and Copper caging of the 90° elbow (Copper – Cu)
- Pipe and 90° elbow (Copper-Chromium-Zirconium – CuCrZr (Treatment B))
- Swirl tape (Copper – Cu)
- Supports (Stainless steel – AISI316L(N))
- Connection weld (Inconel – Alloy 625)
- Fluid (Water – H_2O)

Fig. 2 shows the connection weld with Inconel filler material needed to join the 90° elbow to the central-dome pipe, both made of the same base material (CuCrZr). Inconel connection welds are present at several locations on the pipe, but the weld is only modelled at one of the most thermally loaded locations shown in Fig. 2. The model of the weld is simplified to fit the pipe geometry and the Inconel material properties are considered in the weld. Swirl tapes with a twist ratio of 4 are inserted only in the straight segments of the IVT and OVT pipes (central dome does not have swirl tape). High heat fluxes above 1 MW/m^2 are typical heat loads of PFUs, and high temperatures can therefore be expected. For this reason, temperature-dependent material properties from [23] are considered in the CFD (thermal conductivity, density, specific heat) and thermo-mechanical (Young's modulus, Poisson's ratio, thermal expansion coefficient, yield strength) simulations, as well as in the integrity analyses (uniform elongation, allowable primary membrane stress intensity, ultimate strength). Water properties were taken from IAPWS tables in ANSYS CFX [24]. The thermohydraulic conditions in

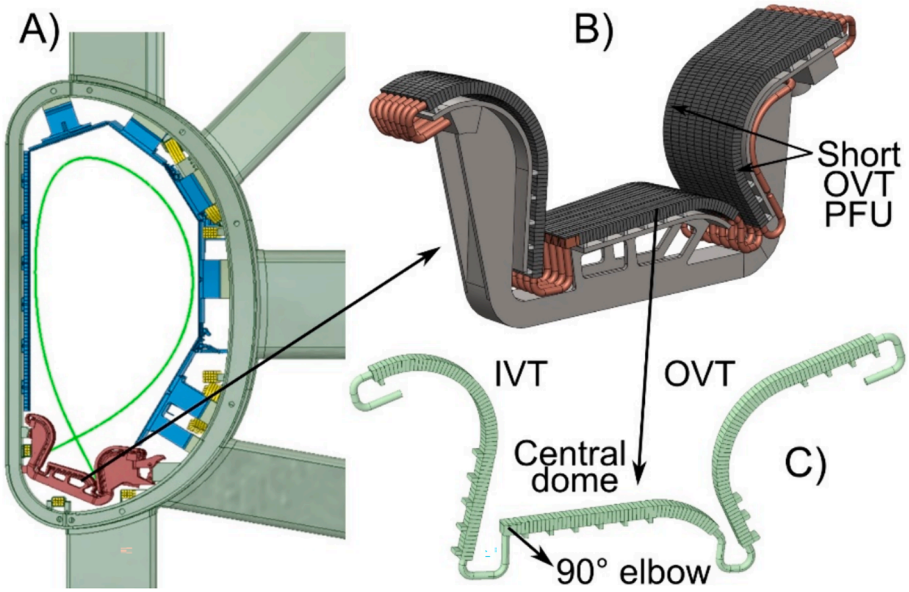

Fig. 1. A) Cross-section view of the DTT reactor. B) Divertor module (cassette with PFUs). C) A single PFU with cooling pipe.

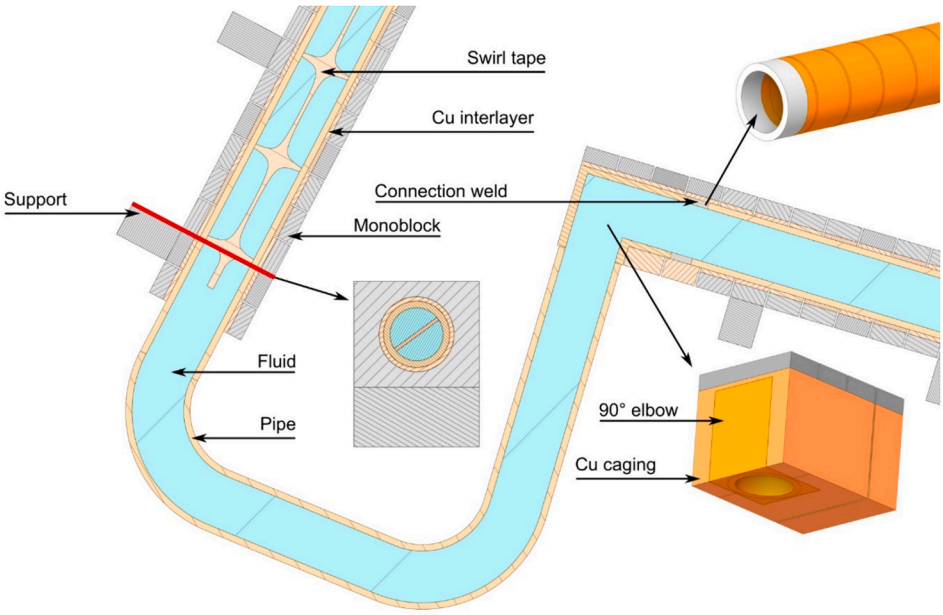

Fig. 2. PFU components between IVT and central dome.

the water pipe are given in Section 3.1.

2.2. Heat loads

Three different heat load scenarios are shown in Fig. 3 for the SN configuration at maximum toroidal field (Bt = 5.85 T) and plasma current (Ip = 5.5 MA), which correspond to different plasma and transport conditions. The thermal loads were evaluated with the 2D axisymmetric edge fluid-kinetic code SOLEDGE2D-EIRENE. The code, starting from conditions imposed on the separatrix, such as the power and its decay length, allows simple management of all magnetic configurations and can resolve the heat load on all the first wall components [25].

Specifically, the three heat load scenarios are: a detached case obtained with neon seeding in the so-called DTT full power scenario in which approximately 45 MW are injected and 28 MW cross the separatrix (Detached, Fig. 3 left); a reduced power case with 14 MW crossing the separatrix with H-mode transport like the previous case (Attached, Fig. 3 middle) and a reduced power case with 7 MW crossing the separatrix but with reduced transport coefficient in Scrape-Off Layer (SOL) and far-SOL such that in the divertor the heat flux is concentrated in a very narrow region (Attached high peak, Fig. 3 right). These three heat loads were selected to study the different localization of the power flowing to the divertor targets. The power values crossing the separatrix are consistent with the surface integrals of the heat flux distributions in Fig. 3, for the three heat load scenarios considered.

Heat flux distributions along the PFU for the three heat loads are presented in Fig. 3. It can be seen that the detached scenario has a more

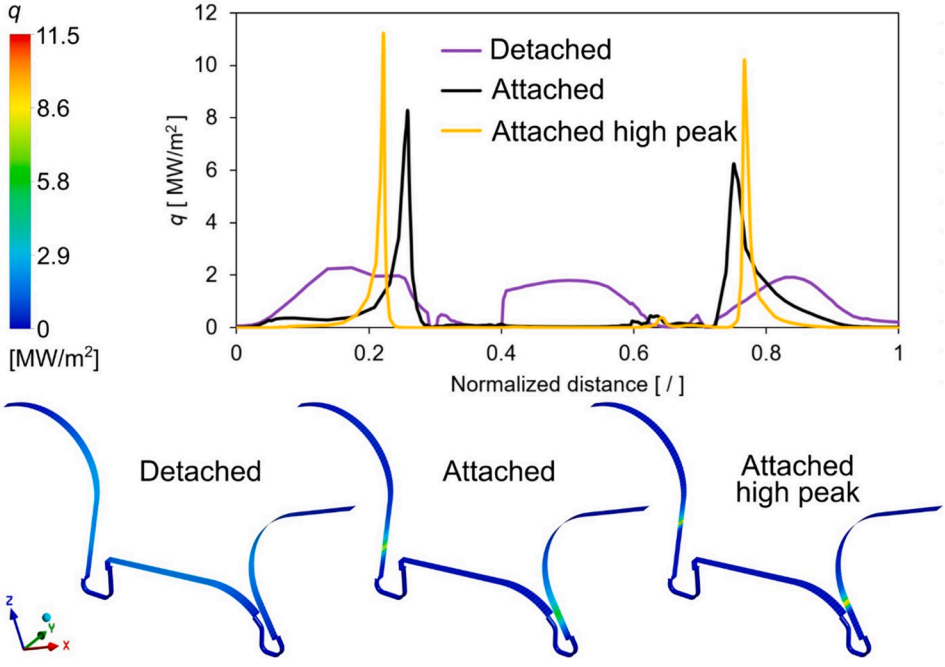

Fig. 3. Heat flux distributions along the PFU loaded surfaces (top) and their surface distributions used as boundary conditions in the CFD simulations (bottom).

uniform distribution of lower heat flux levels, while the two attached scenarios have remarkably high local peaks. The central dome in the detached scenario is also significantly more loaded as compared to the attached scenarios. The heat flux boundary condition is defined on the top surfaces of the monoblocks and does not change in the toroidal direction. On the pipes, a projection of heat fluxes was assumed by a cosine function with the maximum value at the top of the pipe wall and zero at the sides (see Appendix B).

It is worth mentioning that the loads reported in Fig. 3 are the total heat loads deposited on the plasma facing units (radiation + particles). In the full detached scenario, the load is dominated by radiation, while in the attached scenarios the main contribution to the power density is due to the charged particles.

A 3-stage approach to evaluate the structural integrity of the PFU exposed to the above heat flux distributions is described in the next sections together with the presentation of the main results. The analysis includes CFD and thermo-mechanical simulations that are followed by the structural integrity assessment using the codified rules.

3. CFD analysis

3.1. CFD model

The steady-state simulations were set-up using a coupled fluid–solid model, where the heat transfer is solved through all the domains simultaneously. ANSYS CFX 21.2 [24] was used to perform the simulations with finite volume method. In the solid domains, the three-dimensional heat conduction equation was solved and in fluid domain the governing transport equations for mass, momentum and energy equation were solved with the Reynolds Averaged Navier-Stokes (RANS) method. Within RANS, the turbulent flow was solved with the $k-\omega$ Shear Stress Transport (SST) model.

The model meshes shown in Fig. 4 with 9.5 million finite-volume cells were selected using a mesh sensitivity analysis (see mesh 5 in Appendix A.1).

Thermohydraulic boundary conditions

The thermohydraulic boundary conditions in the cooling pipes are based on initial PFU studies [15,16]. Each PFU is cooled by a water pipe with a mass flow rate of 1.186 kg/s and an inlet temperature of 60 °C. The pressure boundary of 5 MPa is specified at the outlet of the pipe. The heat fluxes for the different SN plasma exhaust scenarios (see Section 2.2) were defined on the plasma-facing surfaces (top of monoblocks and pipes) with adiabatic thermal boundaries on all the remaining surfaces.

3.2. CFD simulation results

In this section the CFD simulation results with the different heat loads are presented. The results in Table 1 show the maximum temperatures of solid and fluid domains, average temperatures of monoblocks and fluid, the fluid temperature increase between inlet and outlet (ΔT Inlet-Outlet), the fluid pressure drop (Δp, difference in average pressures between the inlet and outlet of the pipe), as well as the average value of the non-dimensional wall distance (y^+) in the fluid domain. The parameter y^+ is calculated in the first near-wall volumes of the fluid domain and is averaged over all fluid–solid surfaces (in this case the pipe wall and the twisted tape surfaces). A low y^+ value below 5 defines a good near-wall mesh quality, sufficient for a reasonably accurate heat transfer calculation. The results indicate that the local (maximum) temperatures are higher for both attached SN scenarios (at the peaks) as compared to the detached SN scenario, but the overall (average) temperatures are higher in the detached SN scenario. The fluid inlet–outlet temperature difference correlates with the plasma input power (higher

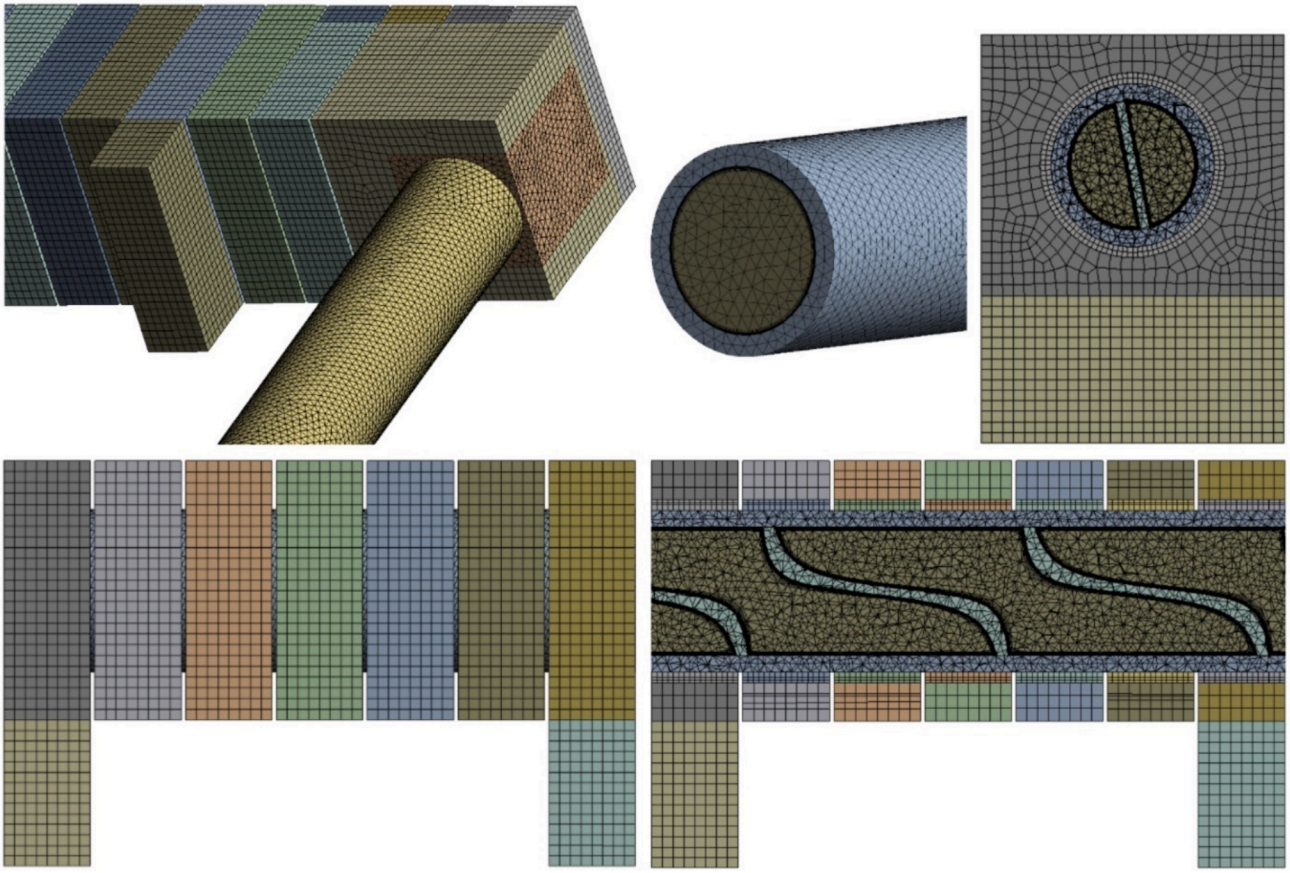

Fig. 4. Finite volume mesh used in the CFD simulations of the PFU.

Table 1
CFD simulation results of the PFU under different heat loads.

Parameter	Units	Heat load		
		Detached	Attached	Attached high peak
T_{max} Monoblock	°C	219.70	551.56	653.71
T_{max} Cu caging		131.01	70.37	63.08
T_{max} Pipe		126.43	192.65	223.43
T_{max} Cu interlayer		133.68	218.57	252.57
T_{max} Supports		83.94	82.27	89.40
T_{max} Connection weld		130.99	65.16	63.08
T_{max} Fluid		109.50	122.36	134.74
T_{avg} Monoblock		92.59	65.32	74.74
T_{avg} Fluid		67.22	63.80	61.98
ΔT Inlet-Outlet		10.36	5.84	3.08
Δp	bar	4.82	5.55	5.56
y^+_{avg}	/	1.15	3.31	3.19

the ΔT, higher the input power). A higher pressure drop occurs in the attached SN scenarios due to the lower temperature (higher viscosity) of the fluid. Parameter y^+ is below 5 for all three scenarios, which indicates that the velocity and temperature profiles in the boundary layer are resolved directly without using wall functions. Temperature distributions of the PFU and of the fluid obtained for the different heat loads are presented in Fig. 5 and Fig. 6, respectively. The local temperature maxima in each segment of the PFU monoblocks are also provided for completeness. It can be observed that the temperature distributions in Fig. 5 are correlated to the heat flux distributions (shown in Fig. 3) on the top surfaces of the monoblocks and pipe. While both attached scenarios show higher local peak temperatures, these occur at the IVT in the attached scenario and at the OVT in the attached high-peak scenario (see Fig. 5). Similar behavior can also be observed in the fluid temperatures in Fig. 6. It is worth mentioning that the temperature drop in the fluid below the Inconel weld (connection weld in Fig. 2) occurs due to the lower thermal conductivity of the Inconel compared to CuCrZr.

The effect of swirl tapes is seen in Fig. 7. As it could be expected, the swirl tapes promote mixing and higher local velocities of the fluid, therefore, enhancing the heat transfer from the heated components to the fluid. Additional mixing and local pressure drop, which promotes higher local velocity, occurs also in the elbow at the end of the central dome due to the sharp corner.

4. Thermo-mechanical analysis

4.1. Thermo-mechanical model

Thermo-mechanical simulations were performed using finite element analysis (FEA). The geometry model of the PFU remained the same as in the CFD simulations with the exception of the fluid domain and swirl tapes which were omitted, since it is assumed that they do not influence the mechanical response of the PFU. Therefore, the geometry in the thermo-mechanical model consisted of five solid domains (monoblocks, Cu interlayer and caging, pipe, supports and connection weld) as defined in Section 2.

The ABAQUS finite element (FE) code was used to perform the FEA [22]. The model meshes with 730 k FE shown in Fig. 8 were selected in a mesh sensitivity analysis (see mesh 7 in Appendix A.2). Hexahedral (C3D20R) with combination of tetrahedral (C3D10R) (in 90° elbow) quadratic FE with reduced integration were employed in the thermo-mechanical model.

For the mesh sensitivity analysis (Appendix A.2), the three-dimensional equations of linear thermo-elasticity were solved. During these analyses, the Cu interlayer located between the pipe and the monoblocks (see Fig. 2) exceeded yield stress on several locations. Therefore, ideal-plasticity constitutive model for the copper components (interlayer and also the caging of the 90° elbow) was assumed in all later simulations.

Two types of loads were considered in the simulations: a fluid pressure of 5 MPa (the same pressure as in CFD analyses) acting on the inner surface and the structural temperature distribution of the solid domains from the CFD results. The stress-free temperature was set to 20 °C. The temperature distribution was defined as an analytical field and then interpolated on the thermo-mechanical model meshes from the CFD meshes using the predefined field tool in ABAQUS environment.

Mechanical boundary conditions

The boundary conditions (BC) were defined on the support surfaces to model the interaction between the PFU and cassette. Each support has a BC defined on the centerline of its bottom surface marked in green in Fig. 9 (top right), which allows rotation of the support. In all supports, the centerline displacement in the local z direction is blocked. Additionally, the displacement in local x direction is also blocked in supports 6, 12 and 13. These boundary conditions simulate a pin-hole type for supports 6, 12, and 13, which prevents axial displacement, and pin-slot

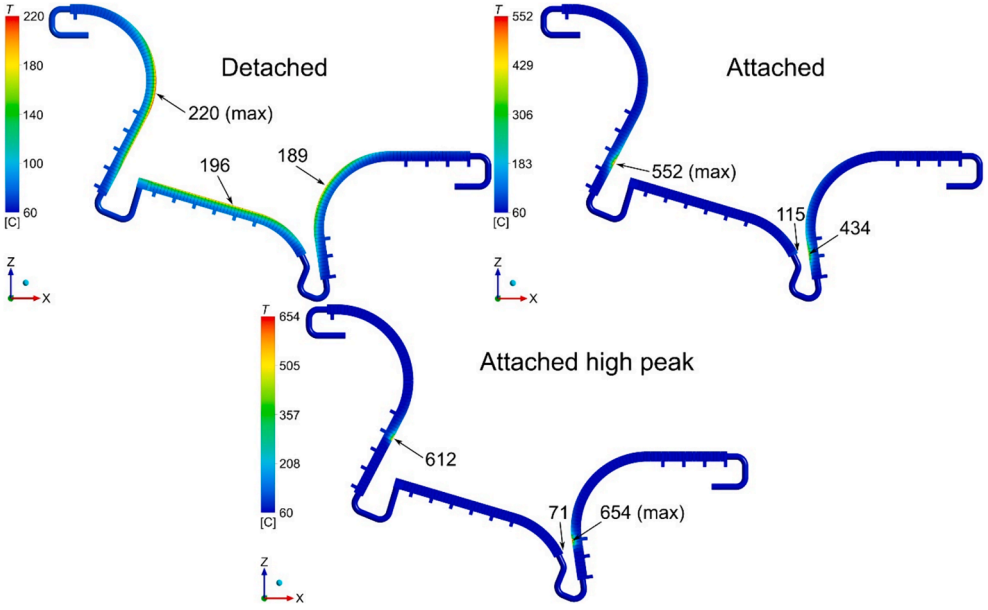

Fig. 5. Temperature distributions of the PFU. Local temperature maxima in each segment of the PFU are marked with arrows.

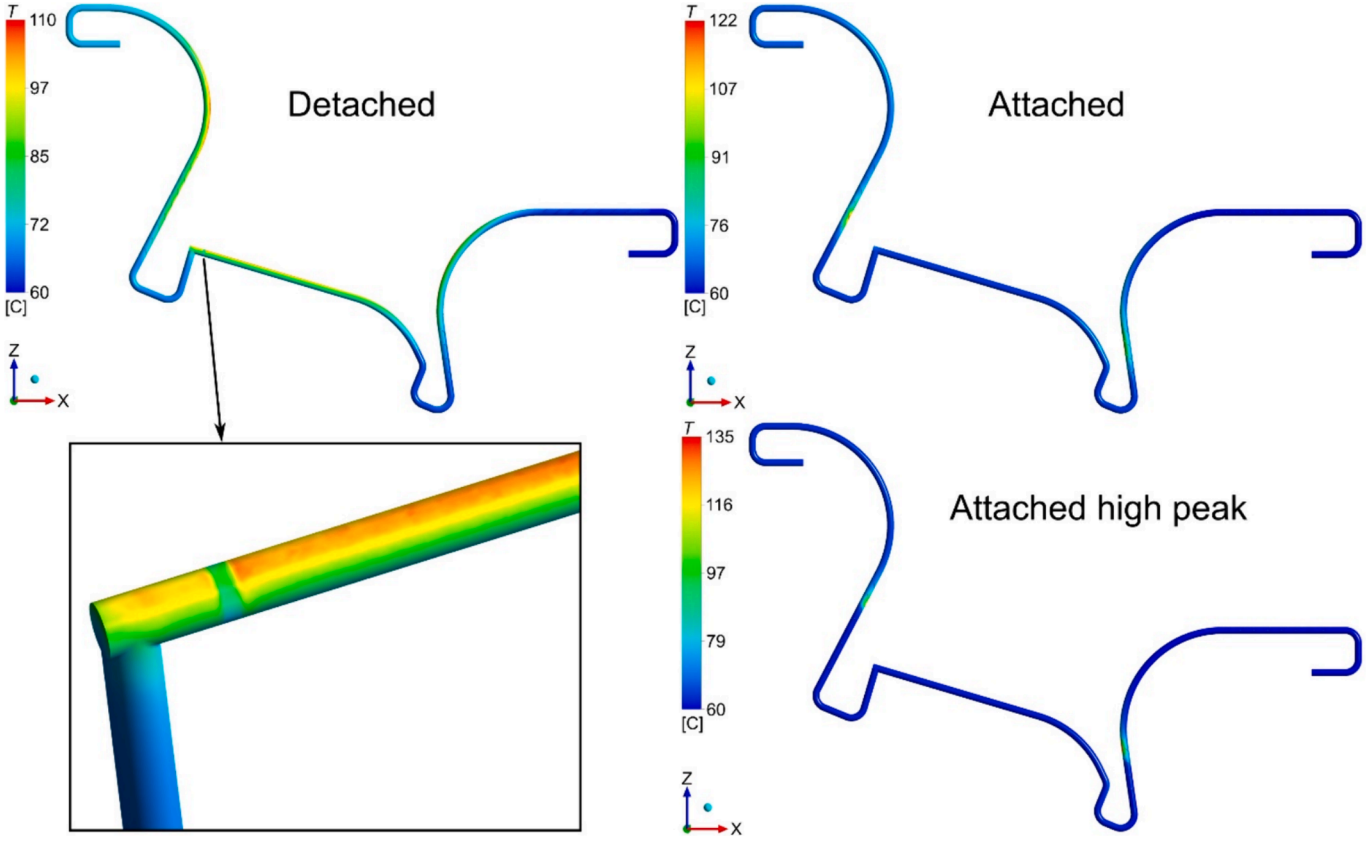

Fig. 6. Temperature distributions of the fluid with a detail below the connection weld (Inconel weld) in the bottom lef.

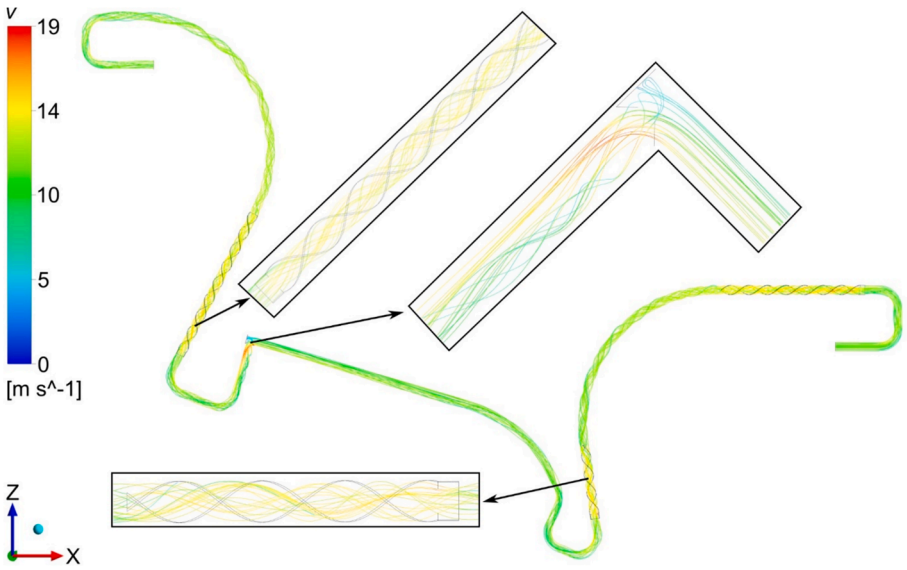

Fig. 7. Velocity streamlines for the detached SN scenario.

type for the other supports, which allows axial displacements to prevent stresses from thermal changes (see Fig. 9 bottom). The local *x* direction is also blocked at the inlet and outlet faces of the pipe, since they are connected to the divertor cassette. The displacement in the toroidal *y* direction is blocked on all of the supports and inlet and outlet faces, on one vertex on the symmetry XZ plane (marked with yellow points in Fig. 9) to prevent free body movement.

4.2. Thermo-mechanical simulations results

4.2.1. Elastic and elasto-plastic analyses for the detached SN scenario

In this section, the detached SN scenario is employed to study the effects on the overall stresses from the use of elastic and elasto-plastic material behavior of the Cu interlayer and Cu caging (ideal plasticity, Section 4.1). The detached SN scenario was selected for this study due to the lower maximum values and higher average values of heat flux (see Fig. 3).

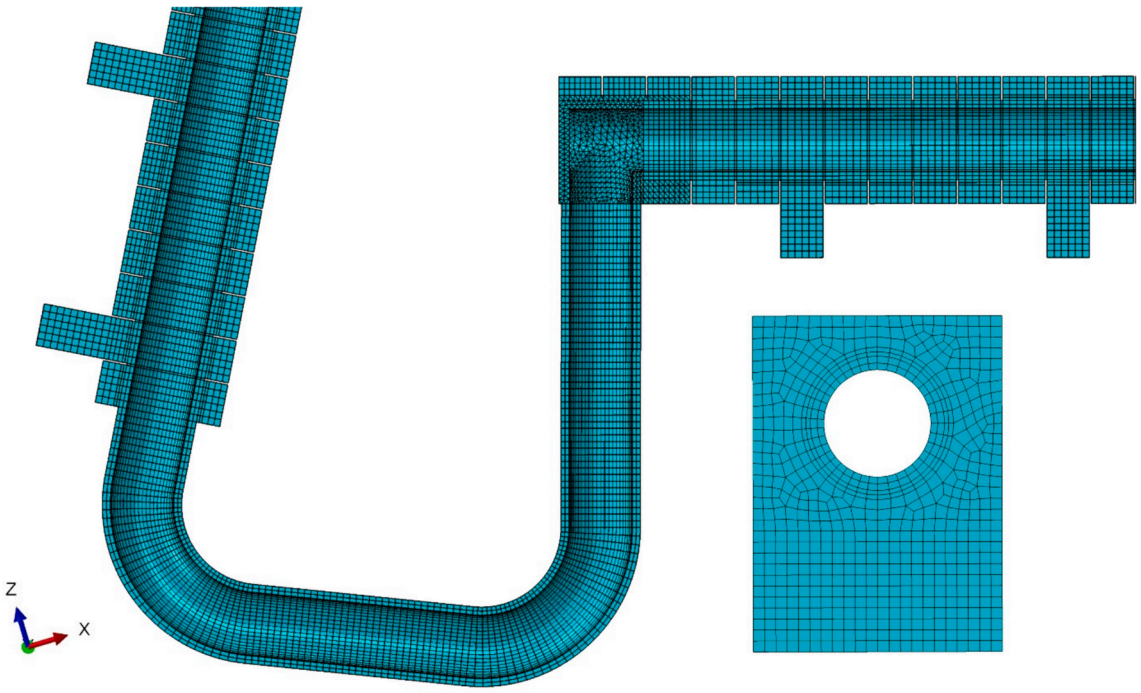

Fig. 8. FE mesh used in thermo-mechanical simulations of the PFU.

Table 2 presents a comparison between the results obtained with elastic and elasto-plastic Cu material properties. The results for the Cu caging and Cu interlayer with elastic material behavior show maximum and average von Mises stresses well above the yield value of approximately 50 MPa (at room temperature). Note that the minimum yield strength $\sigma_{y,min}$ at maximum temperature T_{max} is included in Table 2 for all components, and the corresponding temperatures T_{max} are given in Table 1. When elasto-plastic material properties for Cu are used, the stresses in the caging and interlayer remain near the yield strength of the material. The choice of elastic or elasto-plastic model for Cu also affects the stresses in the other components. As can be seen in Table 2, a significant reduction of maximum stress in monoblocks, pipe and connection weld is observed for the results with elasto-plastic compared to the elastic Cu model. This occurs due the transformation of energy to plastic work instead of increasing the elastic strain. Moreover, Cu is chosen as a functional material between W and CuCrZr specifically for the purpose of mitigating the stresses at the interface between the structural material (CuCrZr) and the plasma-facing material thanks to its low yield stress. The change in Mises stresses is also depicted in Fig. 10, where the Cu caging is highlighted. The maximum stress in the supports is rather close to the yield strength of the stainless steel, but it is limited to a very narrow region in support 12.

The elasto-plastic Cu properties are assumed in all the remaining analyses.

Elasto-plastic analysis of primary and secondary loads

For later use in the integrity analyses, the primary and secondary load types were studied separately using again the detached SN scenario. Note that similar findings were also obtained for both attached SN scenarios, thus these results are not presented here. Three combinations of loads are considered, namely pressure as the primary load, temperature distribution as the secondary load and, in the third case, both loads combined. Note that, for the analysis with pressure load only, a 20 °C constant temperature was considered. The results for the detached SN scenario in Table 3 present the maximum and average Mises stresses obtained in the different PFU components. It can be observed that the temperature distribution is the main contributor to the stresses with combined loads. The contribution of the pressure load is rather small and, in the case of pipe stresses, it even reduces the effect of the secondary loads as it is seen by comparing the maximum stresses between secondary and combined loads for the pipe. Table 3 also shows that the maximum stress in the Cu interlayer is the highest with pressure load alone, due to the material properties evaluated at the lower temperature of 20 °C, where the yield strength is also higher than at higher temperatures.

The displacement magnitudes U, obtained for different load combinations are shown in Fig. 11 (deformation scale factor 100). It can be seen that the largest displacements of 0.47 mm occur due to secondary loads in the curved PFU region and in the Cu caging.

4.2.2. Elasto-plastic analysis of different heat load scenarios

In this section, the effect of the different heat loads on the PFU stresses and displacements is studied assuming elasto-plastic Cu properties. The results in Table 4 show the maximum and average Mises stresses, and reaction forces on the supports in the global x , y and z directions. As it can be seen in Table 4, the average stresses in the monoblocks and Cu interlayer are almost unaffected by the different loads. The maximum stresses in monoblocks range from 258 to 352 MPa, while for Cu interlayer they are almost unaffected (~48.2 MPa) as they have reached the yield strength of Cu. The structural pipe component is locally more loaded in the attached SN scenarios, but on average the detached SN scenario has higher stresses. The reported reaction forces in global directions are the sum of force components from all supports (1–19), obtained individually as a line integral of the directional reaction force along the support centerline. For completeness, Table 4 also presents the magnitude of the total reaction force. From the results in the table, it can be seen that the reaction force in z (vertical) direction is almost identical in all scenarios, while in the y (toroidal) direction is insignificant. The reaction force in x direction is predominant and the highest for the detached plasma scenario.

The Mises stress distributions obtained with the different heat loads are presented in Fig. 12. As observed before, these distributions also show higher overall and local stresses, respectively, in the detached and attached scenarios. There is also a substantial difference in the obtained stresses in the exposed pipes between the scenarios. In the case of the detached SN scenario there are also higher stresses on the pipe elbows (black circles in Fig. 12 top left).

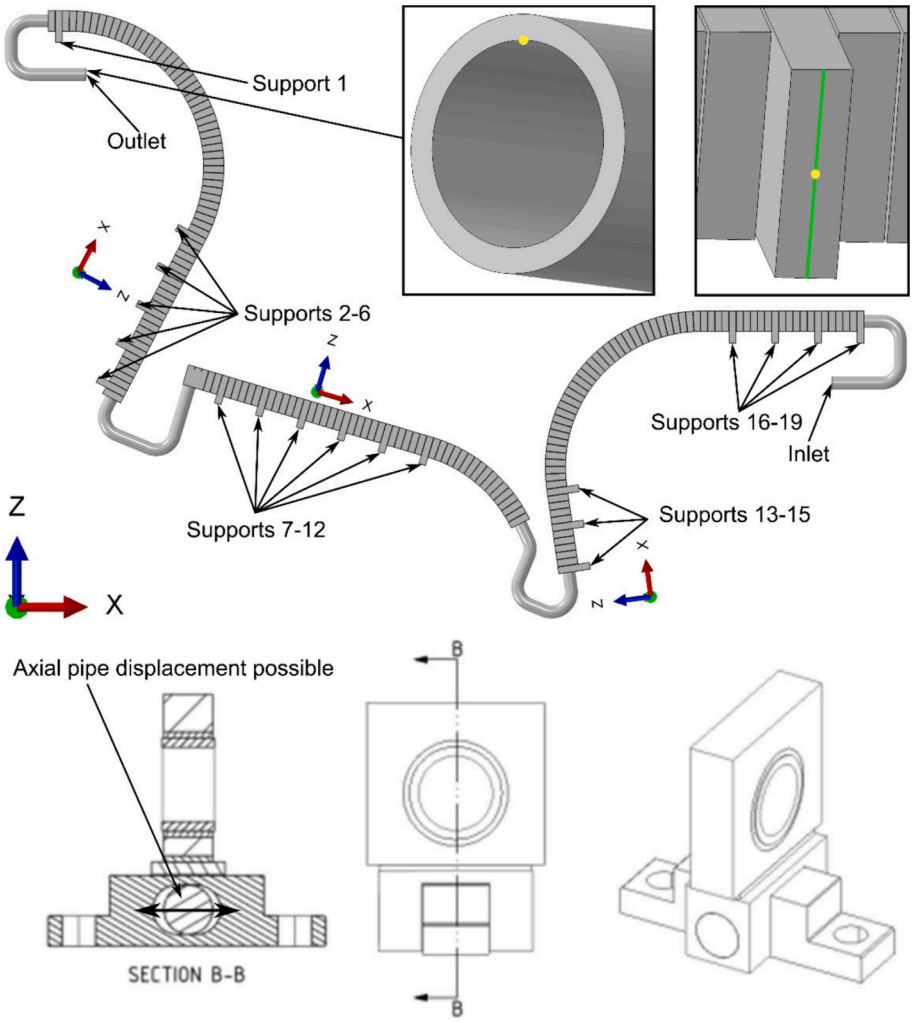

Fig. 9. Boundary conditions in thermo-mechanical simulations (top) and sketch of the PFU pin-slot fixation system to the cassette body for supports 1–19 without 6, 12 and 13 (bottom).

Table 2
Thermo-mechanical results of the PFU for elastic and elasto-plastic material properties for Cu.

Units	MPa				
Parameter	σ_{max}		σ_{avg}		$\sigma_{y,min}$ (T_{max})
	elastic	elasto-plastic	elastic	elasto-plastic	
Monoblock	357.71	258.00	55.85	46.44	1132.71
Cu caging	488.40	47.08	30.19	17.57	43.73
Pipe	210.14	171.32	64.79	67.45	326.01
Cu interlayer	190.64	48.16	80.06	46.50	43.62
Support	169.09	175.75	23.44	23.36	178.40
Connection weld	137.49	130.20	74.13	67.31	390.78

The obtained displacements are shown in Fig. 13 (deformation scale factor of 100). The overall deformed shapes are very similar for the different plasma scenarios, and the highest displacements of 0.47 mm are achieved in the detached scenario. The inner vertical target seems to undergo rather high bending displacements as this long portion of the PFU does not have fixing supports. Fig. 13 (bottom left) presents a detail of the rotations undergone by the supports with dedicated modeling (Section 4.1).

5. Structural integrity evaluation

The displacements, strains and stresses calculated by FEA at selected locations are analyzed with design criteria to evaluate the structural integrity of the PFU components. The Structural Design Criteria for In-vessel Components (SDC-IC) are used in this study [20]. These criteria ensure that the required safety margins are met for the different types of mechanical damage, which are evaluated using elastic and elasto-plastic analyses.

The selected locations are studied on a supporting line segment – a line defined between the two outside surfaces perpendicular to at least one of them – as shown schematically in Fig. 14 (right). For the elastic material, a linearization of the stress on the line segment is performed as shown in Fig. 14 (left), and broken down into membrane (average), bending (linear) and non-linear stresses. For the elasto-plastic copper material, a strain linearization is performed, since the yield strength of the material is exceeded (see Table 2) and the stress linearization is no longer accurate.

The rules used in this study are part of the "Low-temperature rules" (IC 3100). These are selected on the basis of the so-called Negligible thermal creep test (IC 3050). Based on previous studies [26], it was concluded that thermal creep is not relevant and low-temperature rules are sufficient for the analyses considered in this paper.

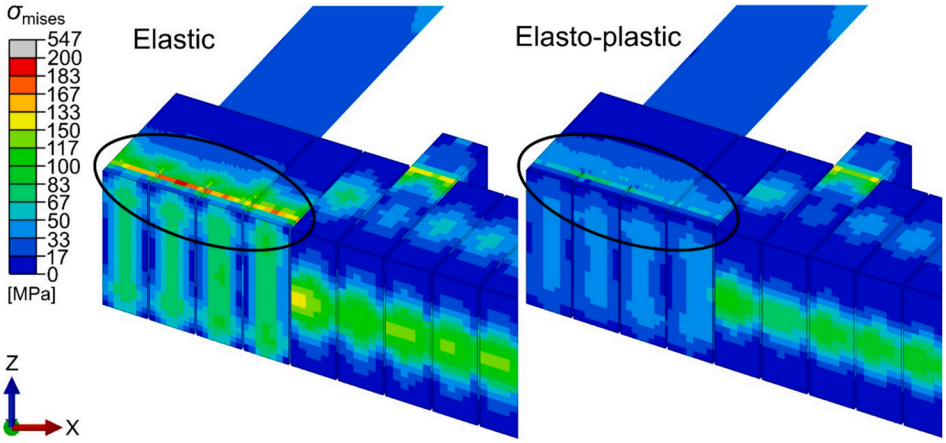

Fig. 10. Mises stresses in the PFU obtained with elastic and elasto-plastic material properties for Cu[11].

Table 3
Thermo-mechanical results of the PFU for different load combinations in detached SN scenario.

Parameter		Units	Load		
			pressure only (primary)	temperature only (secondary)	Combined
Monoblock	σ_{max}	MPa	36.55	255.48	258.00
	σ_{avg}		4.21	42.50	46.44
Cu interlayer	σ_{max}		55.00	48.16	48.16
	σ_{avg}		5.25	46.52	46.50
Pipe	σ_{max}		81.15	176.75	171.32
	σ_{avg}		12.03	67.25	67.45
Connection weld	σ_{max}		16.44	118.68	130.20
	σ_{avg}		11.64	60.87	67.31
Support	σ_{max}		25.02	170.07	175.75
	σ_{avg}		0.90	23.56	23.36

5.1. Elastic analysis

Initially, the evaluation was performed using the M-type ("monotonic load") criteria at level A (operating and upset conditions). Several criteria were considered: Immediate plastic collapse and plastic instability (primary membrane and bending stress IC 3121.1.1.2a and local primary membrane stress IC 3121.1.1.3) and Immediate plastic flow localization (primary plus secondary membrane stress IC 3121.2.1.1). Except for the latter, these criteria use only primary stresses. However, the simulations in Section 4.2.1 show that primary loads are not dominant. The later criterion also uses secondary loads, but only the local primary membrane stress is considered. It is therefore less stringent than the $3S_m$ rule, presented next. Similarly, the Immediate plastic flow localization criterion has very high allowable stresses for ductile materials (one order of magnitude or higher than calculated stresses) and it is usually not needed in the analyses, except for the cases where the material is likely to suffer severe embrittlement. Due to these reasons, the so-called $3S_m$ rule (IC 3131.1.2) presented in Eq. (1) is the chosen criterion in the elastic analysis. This criterion compares the obtained stresses with the allowable stress. It consists of primary membrane stress P_L, primary bending stress P_b and local secondary stress Q_L. The first two stresses are defined in Section 5 (Fig. 14) and are the consequence of a mechanical load (pressure). The last stress is the consequence of the temperature distribution in the component. The right-hand side of Eq. (1) is an allowable primary membrane stress intensity S_m and it is defined as a fraction of yield or ultimate strength, which depends on a

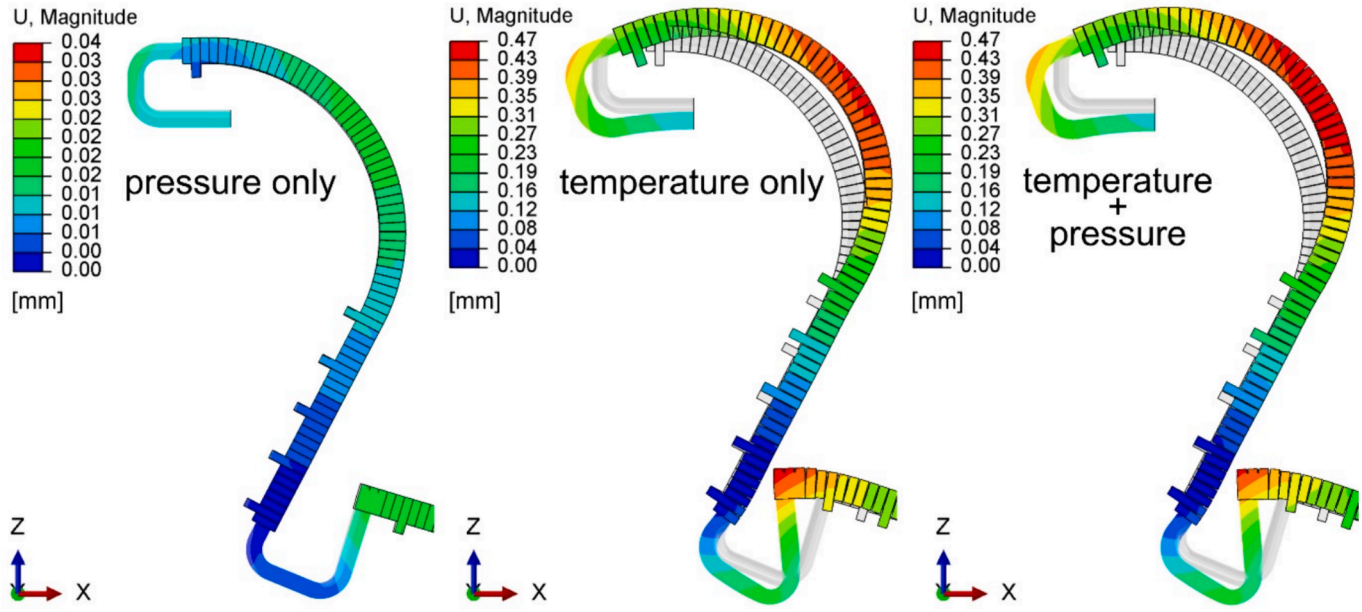

Fig. 11. Displacements of the PFU with primary and secondary loads, deformation scale factor 100.

Table 4
Thermo-mechanical results of the PFU for different heat loads.

Parameter		Units	Heat load		
			Detached	Attached	Attached high peak
Monoblock	σ_{max}	MPa	258.00	326.24	352.04
	σ_{avg}		46.44	42.03	40.60
Cu interlayer	σ_{max}		48.16	48.20	48.20
	σ_{avg}		46.23	47.21	47.30
Pipe	σ_{max}		171.32	193.82	215.77
	σ_{avg}		67.45	55.00	50.71
Connection weld	σ_{max}		130.20	74.79	71.84
	σ_{avg}		67.31	43.26	41.85
Support	σ_{max}		175.75	156.27	149.45
	σ_{avg}		23.36	20.99	20.26
F_x		N	−495.76	−357.89	−334.6
F_y			−2.5	−0.16	−0.82
F_z			159.13	160.14	160.28
F_{mag}			520.68	392.08	371.01

detached SN scenario, locations 1 – 2 are positioned in-between the monoblocks, where stress concentrations can be expected [27], while in both attached scenarios, locations 3 – 6 are roughly positioned on the pipe below the center of the monoblocks.

Three locations on Cu interlayer were also selected for each of the SN scenarios. For both attached scenarios, two of these locations undergo the highest Mises stresses in the Cu interlayer (locations 10, 11, 13, 14), due to the highest temperatures observed in IVT and OVT. One additional location in the central dome (locations 12, 15), which is out of the critical zones with near-average Mises's stress, is also selected for completeness. For the detached SN scenario, the procedure is reversed and one location corresponds to the highest temperature and Mises's stress (location 7) and two with near-average stress values (locations 8 and 9). These two later locations were selected on the IVT (with high stress) and on the central dome (average stress), to represent different targets.

In Fig. 15, the specific position of line-segments where the assessment is performed for the different locations is shown through letters in the cross-sectional views of the Cu interlayer (a-d) and CuCrZr pipe (A-B).

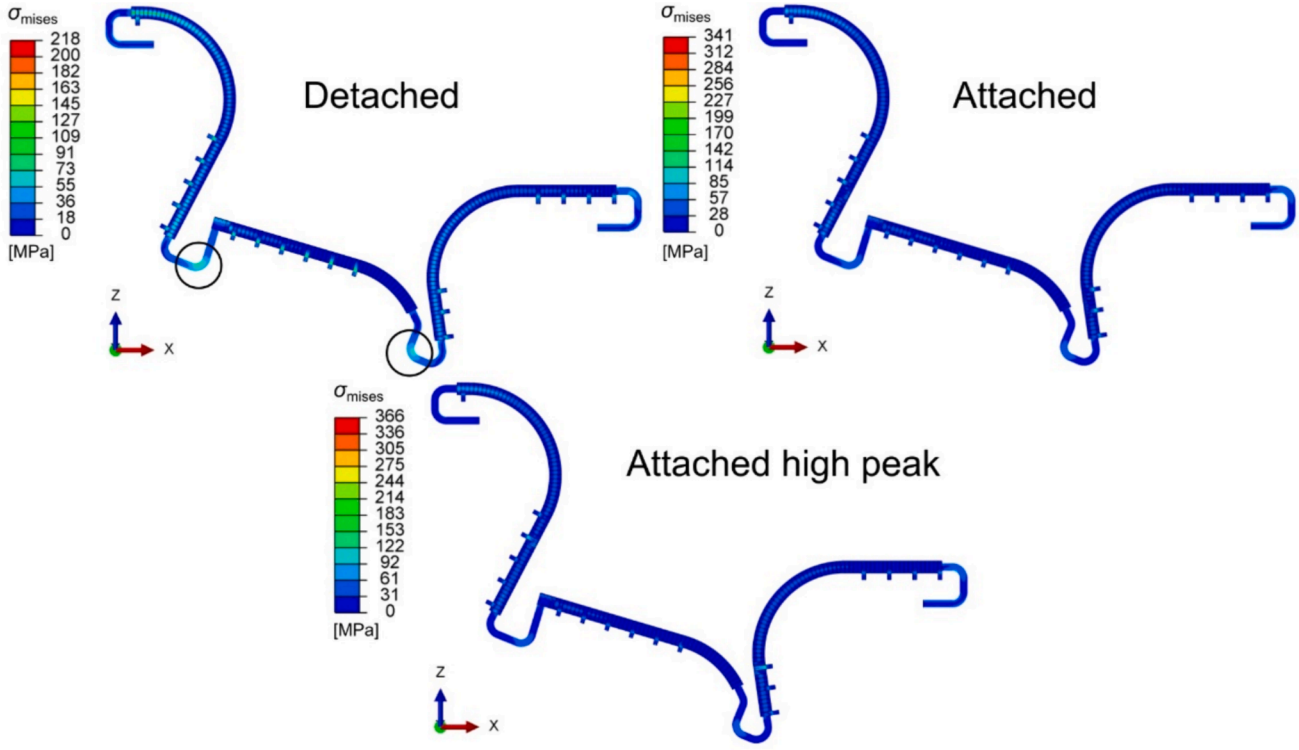

Fig. 12. Mises stress distributions on the PFU for different heat loads[1].

material of choice [23]. Like all other material properties, S_m is also temperature dependent.

$$\overline{P_L + P_b + Q_L} \leq 3S_m \quad (1)$$

The chosen locations for the different plasma scenarios are presented in Fig. 15, and the results of the integrity analyses through the $3S_m$ rule (Eq. (1)), are presented in Table 5. Locations 1 – 6 correspond to line segments through the pipe thickness where the highest temperatures (in the pipe) were obtained and, consequently, the stresses are also (in most cases) the highest. These locations belong to IVT and OVT. In the

For each scenario and location, the results in Table 5 provide the computed values for the left-hand side of the inequality in Eq. (1), the $3S_m$ value (material and temperature dependent), the quotient of these two numbers (referred to as failure fraction) and the answer to whether the criterion is fulfilled or not. As it can be observed in the table, the criterion for the pipe is fulfilled at all locations. It is worth mentioning that the selected treatment B for the CuCrZr pipe material is more conservative due to its lower strength as compared to treatment A [23]. Following this design criterion, material treatment B is thus sufficient, although the obtained Mises stress is higher than the yield strength under attached plasma scenarios at the spots with localized heat fluxes (locations 3, 5, 6). If treatment A would be chosen, the yield strength would not be exceeded. The results in Table 5 also show that the criterion is fulfilled at none but 2 of the Cu interlayer locations. Therefore,

[1] Stresses in tables and text are computed at FE integration points and stresses in figures are extrapolated from integration points to the model surfaces with quilt contours. This results in differences between maximum stresses in tables, text and figures.

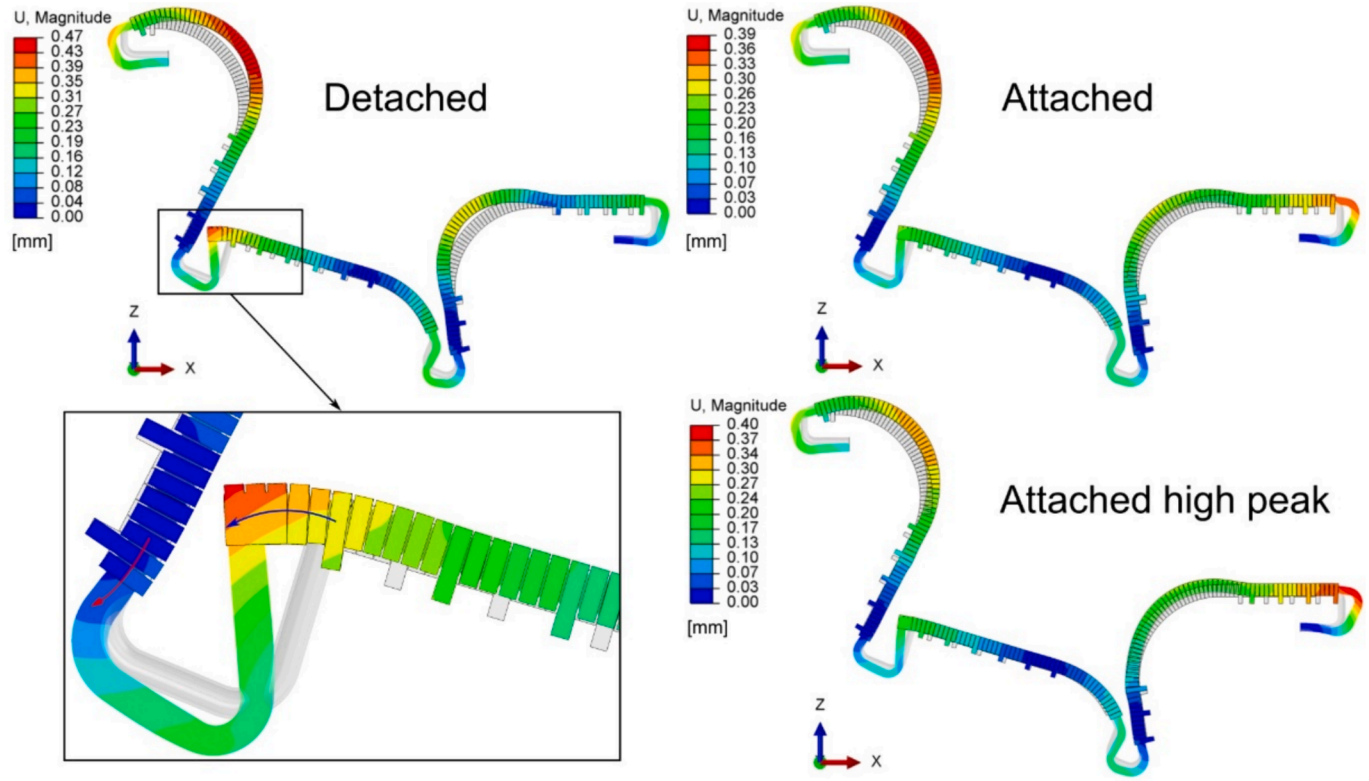

Fig. 13. Displacements of the PFU with different heat loads, deformation scale factor 100.

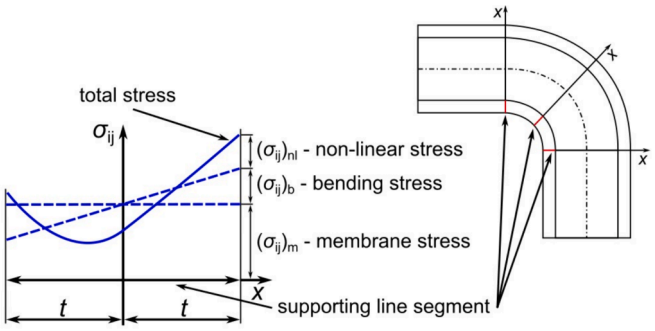

Fig. 14. Stress linearization (left) and supporting line segment (right) – summarized from [20].

elasto-plastic analyses are needed.

5.2. Elasto-plastic analysis

The evaluation has been performed on the basis of several elasto-plastic (damage) criteria. Only selected results are presented here as most criteria proved to not be relevant for the studied conditions, i.e., the calculated plastic strains were at least an order of magnitude smaller than the values allowed by the criteria. These criteria are: Local fracture, exhaustion of ductility (IC 3121.3.2) and Significant mean plastic strain (IC 3131.2.1). Instead of the equations in SDC-IC for the former criterion, another criterion from the ASME – Boiler and Pressure Vessel Code (BPVC) for Local Strain Limit (BPVC section 5.3.3) as defined in [28] was used. The criterion that has not been followed is the Immediate plastic collapse (IC 3121.1.2). As it has been explained in [27], the plastic collapse under normal operating conditions (thermal load cases) is not a driving design failure in the case of the monoblock PFU. This criterion is applicable when upset conditions are considered (electro-magnetic load cases).

The selected criterion is the immediate plastic flow localization (IC 3121.2.2) defined by Eq. (2), which also includes necking. The principal strains are calculated from linearized strain tensor components, and the maximum principal plastic strain is used (significant mean plastic strain $\left(\tilde{\varepsilon}_m\right)_{pl}$). The allowable strain is defined by the minimum uniform elongation $\varepsilon_{u,min}$, which represents the plastic component of the engineering strain at the beginning of the necking. In this work, the average uniform elongation from [23], which is a material and temperature-dependent property, was used as the allowable strain. This criterion also requires applying the so-called load factors (LF) to the thermo-mechanical simulations' inputs before running. These are defined as 2.5 and 1.5 for mechanical loads (pressure) and heat loads (temperature), respectively.

$$\left(\tilde{\varepsilon}_m\right)_{pl} \leq \frac{\varepsilon_{u,min}}{2} \tag{2}$$

The results of the structural integrity analyses performed under the assumption of elasto-plastic behavior of copper components in the thermo-mechanical analyses are presented in Table 6. Three locations on the Cu interlayer were chosen for each plasma scenario as depicted in Fig. 16. Similarly to elastic analysis, two locations with the highest equivalent plastic strains and temperatures (locations 4, 5, 7, 8) and one with near-average values (locations 6, 9) were selected for the attached scenarios. For the detached SN scenario, the location with the highest value of equivalent plastic strain on each of the segments (inner vertical target, central dome, outer vertical target) was chosen (locations 3, 1, 2 respectively).

In Fig. 16, the specific position of line-segments where the assessment is performed for the different locations is shown through letters in the cross-sectional views of the Cu interlayer (a-e).

For each scenario and location, the results in Table 6 provide the computed values for the left-hand side of the inequality in Eq. (2), the allowable strain $\varepsilon_{u,min}$ value (material and temperature dependent), the

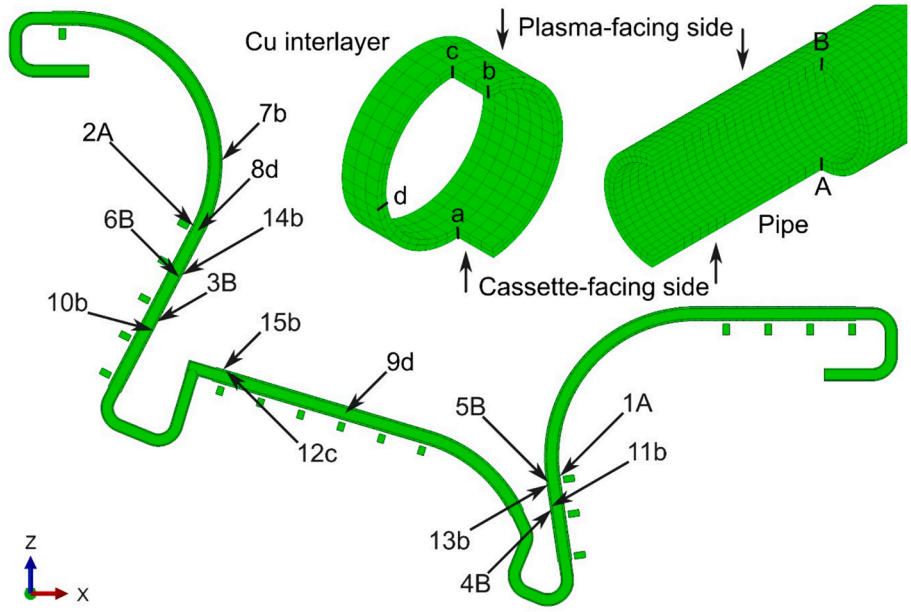

Fig. 15. Locations of supporting line segments for elastic analysis. Letters in cross-sectional views of the Cu interlayer (a-d) and CuCrZr pipe (A-B) define exact position of line segments where assessment is performed for the different locations.

Table 5
Structural integrity results – elastic analysis.

Heat load		Pipe		Cu interlayer		
Detached	Location:	1	2	7	8	9
	$\overline{P_L + P_b + Q_L}$	181.94	185.88	197.94	120.59	128.64
	$3S_m$	369.00	369.00	86.42	91.10	91.69
	Yes/No	Yes	Yes	No	No	No
	Failure fraction	0.49	0.50	2.29	1.32	1.40
Attached	Location:	3	4	10	11	12
	$\overline{P_L + P_b + Q_L}$	231.61	207.26	313.22	259.52	59.23
	$3S_m$	341.82	350.85	81.04	82.33	96.44
	Yes/No	Yes	Yes	No	No	Yes
	Failure fraction	0.68	0.59	3.87	3.15	0.61
Attached High peak	Location:	5	6	13	14	15
	$\overline{P_L + P_b + Q_L}$	283.36	229.71	373.81	313.27	80.97
	$3S_m$	331.32	346.02	72.19	80.22	96.72
	Yes/No	Yes	Yes	No	No	Yes
	Failure fraction	0.86	0.66	5.18	3.91	0.84

Table 6
Structural integrity results – elasto-plastic analysis.

Heat load		Cu interlayer		
Detached	Location:	1	2	3
	$\left(\tilde{\varepsilon}_m\right)_{pl}$	0.0665	0.0274	0.0237
	$\varepsilon_{u,min}/2$	0.1822	0.1867	0.1588
	Yes/No	Yes	Yes	Yes
	Failure fraction	0.36	0.15	0.15
Attached	Location:	4	5	6
	$\left(\tilde{\varepsilon}_m\right)_{pl}$	0.0443	0.0230	0.0023
	$\varepsilon_{u,min}/2$	0.1866	0.1863	0.1862
	Yes/No	Yes	Yes	Yes
	Failure fraction	0.24	0.12	0.01
Attached High peak	Location:	7	8	9
	$\left(\tilde{\varepsilon}_m\right)_{pl}$	0.0253	0.0155	0.0146
	$\varepsilon_{u,min}/2$	0.1186	0.1289	0.1869
	Yes/No	Yes	Yes	Yes
	Failure fraction	0.21	0.12	0.08

quotient of these two numbers (referred to as failure fraction) and the answer to whether the criterion is fulfilled or not. The results show that the criterion is fulfilled in all cases, even at the critical locations 4, 5, 7 and 8 (with predicted high temperature and plastic strain). Interestingly, the highest failure fraction of 0.36 is obtained at location 1 with the detached SN scenario.

6. Conclusions

Detailed computational fluid dynamics and thermo-mechanical simulations of the DTT divertor PFU with realistic heat loads of three plasma scenarios were performed. The steady-state CFD simulations employed a coupled fluid–solid model and an optimized mesh density, selected by mesh sensitivity analysis. The solid domain in the CFD model included different PFU components with different materials, as well as the swirl tape to increase the near-wall velocity, mixing and heat transfer in the fluid domain. The CFD results include the fluid pressure drop (~5 bar), maximum fluid temperature (110 to 135 °C) and the increase in average fluid temperature (3 to 10 K). The obtained temperatures of the PFU components include maximum monoblock temperatures ranging from 220 °C for the detached and 654 °C for the attached high peak plasma scenarios.

The displacements, stresses and strains in the different PFU components have been obtained using thermo-mechanical simulations, taking into account the temperature distribution in the solid calculated by CFD simulations, the pressure load in the fluid and the modeling of the supports. Here again, an optimized mesh density was selected by a mesh sensitivity analysis. Linear-elastic and elasto-plastic material properties were employed to account for local yielding in the copper components. The maximum Mises stresses on the monoblocks between 258 MPa (for the detached scenario) and 352 MPa (attached high peak) were found, with global displacements ranging between 0.39 mm (attached) and 0.47 mm (detached).

Finally, the thermo-mechanical results were compared against design criteria (SDC-IC) for structural integrity analyses. The outcome of these analyses showed that for the elastic behavior of PFU materials, the structural pipe component fulfills the presented $3S_m$ rule (SDC-IC IC 3131.1.2), while the Cu interlayer does not. By evaluating the design criteria with respect to the elasto-plastic behavior of Cu components, it was found that although the interlayer experiences local yielding, the

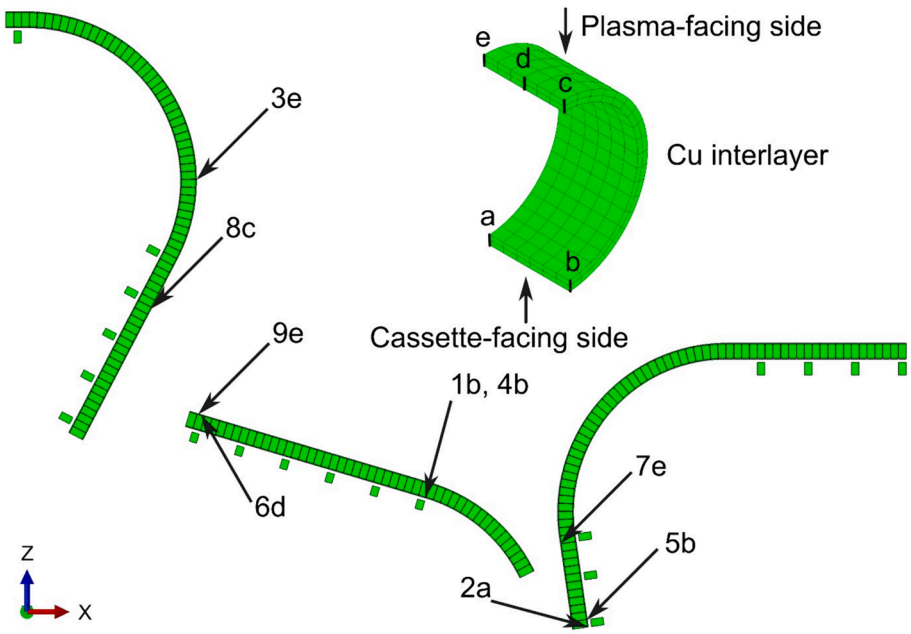

Fig. 16. Locations of supporting line segments for elasto-plastic analysis. Letters in cross-sectional views of the Cu interlayer (a-e) define exact position of line segments where assessment is performed for the different locations.

relevant criteria for immediate plastic flow localization are met (SDC-IC IC 3121.2.2).

CRediT authorship contribution statement

Patrik Tarfila: Writing – review & editing, Writing – original draft, Visualization, Validation, Methodology, Investigation, Formal analysis. **Oriol Costa Garrido:** Writing – review & editing, Supervision, Methodology, Investigation, Formal analysis, Conceptualization. **Boštjan Končar:** Writing – review & editing, Supervision, Funding acquisition, Conceptualization. **Emanuela Martelli:** Project administration, Conceptualization. **Francesco Giorgetti:** Writing – review & editing, Resources. **Selanna Roccella:** Writing – review & editing, Supervision, Resources.

Declaration of competing interest

The authors declare that they have no known competing financial interests or personal relationships that could have appeared to influence the work reported in this paper.

Data availability

Data will be made available on request.

Acknowledgements

This work has been carried out within the framework of the EUROfusion Consortium, funded by the European Union via the Euratom Research and Training Programme (Grant Agreement No. 101052200 - EUROfusion). Views and opinions expressed are however those of the author(s) only and do not necessarily reflect those of the European Union or the European Commission. Neither the European Union nor the European Commission can be held responsible for them.

The financial support from the Slovenian Research and Innovation Agency grants P2-0405, P2-0026 and PR-12902 is gratefully acknowledged.

Appendix

Appendix A. Mesh Sensitivity Analyses

Appendix A.1. Computational fluid dynamics simulations

The mesh density for the CFD model was selected with a mesh sensitivity analysis on a "reduced" model of the PFU (Fig. A1). The reduced model is composed of five monoblocks and Cu interlayer, one pipe and a swirl tape with one turn (360°). Swirl tape is especially important, since it was used to define the mesh in the boundary layer in the fluid near the pipe wall. The main purpose of using a reduced model is to achieve, with shorter calculation times, mesh convergence and, hence, determining the mesh parameters for the whole PFU model. The same boundary conditions as in the whole model (Section 3.1) where employed in the sensitivity analyses with the reduced model, with the only difference of a uniform heat flux of 5 MW/m^2 applied on the top monoblock surfaces.

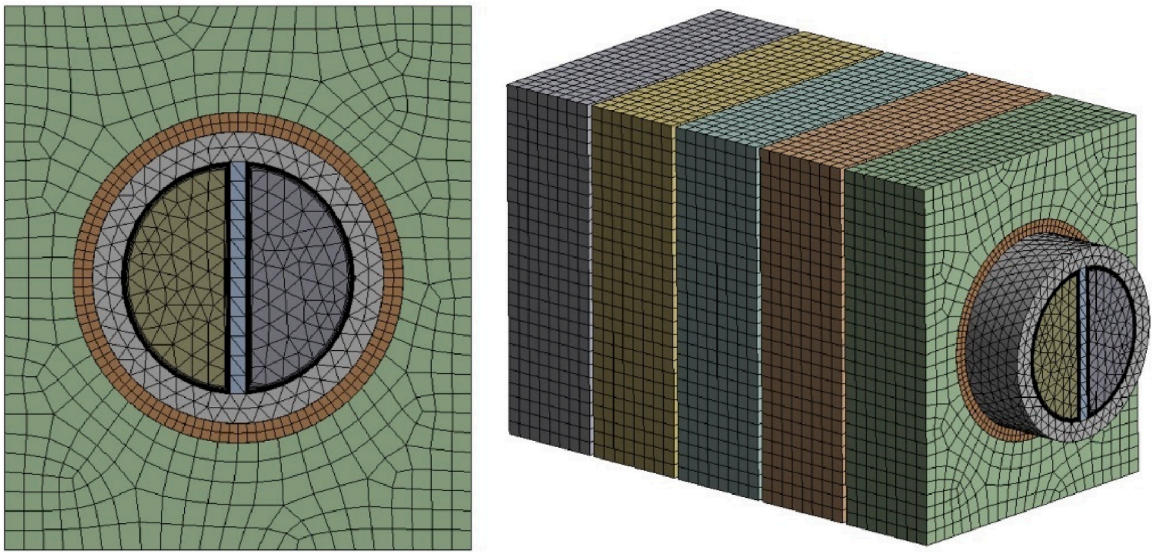

Fig. A1. Finite volume mesh of the reduced model.

Several meshes were tested for mesh convergence as presented in Table A1. The main mesh parameters include finite volume (FV) sizes and inflation layers (first layer height, maximum number of layers and growth rate). An extra fine mesh – number 8 in Table A1 – was developed to confirm the height of first boundary layer.

Table A1
Mesh parameters used in sensitivity analysis for CFD simulations.

	Units	mm					/			
	Parameter:	FV size					Inflation layers			Num. of FV
		C	P	S	F	M	First layer height	Max. num. of layers	Growth rate	
1	extra coarse	0.5	1	1	1	1	0.01	15	1.3	184,839
2	coarser	0.5	1	1	1	1	0.005	18	1.3	203,334
3	coarse	0.5	1	1	1	1	0.005	20	1.25	217,797
4	medium	0.5	1	1	1	1	0.003	20	1.25	225,475
5	fine	0.5	1	1	1	1	0.001	20	1.25	236,994
6	finer	0.4	0.75	0.5	0.75	0.75	0.001	22	1.2	528,943
7	extra fine 1	0.25	0.5	0.5	0.75	0.5	0.001	22	1.2	875,406
8	extra fine 2	0.5	0.75	1	0.5	1	0.0005	20	1.25	948,133

Abbreviations: C – Cu interlayer, P – Pipe, S – Swirl tape, F – Fluid, M – Monoblock, FV – Finite Volume.

Results from the mesh sensitivity are presented in Table A2, including maximum and average temperatures in monoblocks and fluid, and maximum and average values of parameter y^+, for the different mesh densities. Fig. A2 shows the mesh sensitivity convergence through the maximum temperatures in monoblocks and fluid as a function of mesh density. From Table A2 and Fig. A2 it can be observed that the values are rather converged after the mesh 5 (red dot in Fig. A2). Meshes 1–3 have big discrepancies from meshes 4–8, but they also have the least amount of FV. Between meshes 5 and 8, the difference is in order of a few %, but the number of FV is around 4 times smaller for the mesh 5 compared to mesh 8. Therefore, the chosen mesh was number 5, the parameters of which were used to mesh the whole PFU model leading to a total of 9.5 million FV.

Table A2
Results of the mesh sensitivity analysis for CFD simulations.

	Units	°C				/		
	Parameter	T_{max}		T_{avg}		$y+$		Num. of FV
		Monoblock	Fluid	Monoblock	Fluid	Max	Avg	
1	extra coarse	400.8	77.24	149.04	60.57	46.67	30.3	184,839
2	coarser	398.75	86.29	148.29	60.58	23.91	15.28	203,334
3	coarse	398.62	86.39	148.23	60.58	24.55	15.41	217,797
4	medium	396.86	93.65	147.45	60.59	15.32	9.3	225,475
5	fine	395.58	97.35	147.15	60.59	14.92	7.84	236,994
6	finer	395.4	96.59	146.24	60.58	16.15	8.15	528,943
7	extra fine 1	394.64	95.75	145.79	60.58	16.14	8.14	875,406
8	extra fine 2	394.01	101.34	145.88	60.56	18.7	8.37	948,133

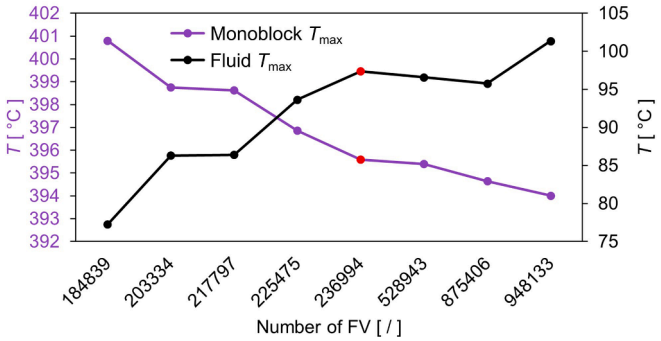

Fig. A2. Mesh sensitivity convergence for CFD simulations.

Appendix A.2. Thermo-mechanical simulations

Similarly to the CFD simulations, a mesh sensitivity was performed with the thermo-mechanical model to select an optimal mesh density. This time, however, the whole model was used with the detached SN scenario as a heat load, and linear-elastic material properties were assumed for all the components. Mesh parameters are presented in Table A3, and they are defined as a global or local finite element (FE) size. The number of FE through thickness in the Cu interlayer and pipe are also presented. In meshes 1 to 3, there is only one FE through pipe thickness, which was then increased to 2 and then 3 in the meshes 4 to 8 to study their influence on the stress distribution through thickness. For the same reason, the number of FE through thickness in the Cu interlayer is increased from 1 to 2 and 4, respectively, in meshes 7 and 8.

Table A3
Mesh parameters used in sensitivity analysis for thermo-mechanical simulations.

	Units	mm		/		/
	Parameter	FE size		Num. of FE through thickness		Num. of FE
		Global	Tetrahedral	Cu interlayer	Pipe	
1	extra coarse	4	/	1	1	64,907
2	coarse	2.5	/	1	1	92,314
3	medium	1.5	/	1	1	345,509
4	fine	1.25	1	1	2	677,796
5	finer	1	0.75	1	3	1,505,875
6	extra fine	0.75	0.6	1	3	3,218,733
7	fine 2	1.25	1	2	2	728,489
8	fine 3	1.25	1	4	2	829,916

The results of the mesh sensitivity are presented in Table A4, through the maximum and average Mises stresses obtained in the PFU components and for the different mesh densities. Note that stress convergence is reported here, since the convergence on displacements is achieved much faster. Average stresses are converged from mesh 4 on, but maximum stresses are still rising on most of the components, especially in monoblocks, Cu caging and pipe. Additionally, the maximum stress progression is presented in Fig. A3. The maximum stress increases for denser meshes due to the so-called edge effect, which describes a stress concentration on the edge or on the border between 2 components. In our case, this happens on the border between monoblocks and Cu interlayer, Cu interlayer and pipe and monoblocks and supports. The main cause for this is the difference in thermal expansion coefficient of neighboring components and, e. g., the Cu interlayer wants to expand more than monoblock allows it to. This can be eliminated by modeling the interaction between the components (friction), but in our case the components are assumed welded to each other.

Fig. A4 presents a comparison of the results with three monoblock meshes (meshes 1, 4 and 6). The legend is fixed to the highest value of mesh 1 for better representation of the growing stress concentration and stress distribution between the coarsest and finest mesh. It can be observed that the stress concentrations are very localized at the monoblock edges and its hole. It can also be noticed that the stress distribution, however, is very similar for meshes 4 and 6, although the number of FE in mesh 4 is almost 5 times lower. Due to this reason and because calculation times are much shorter, mesh 4 was chosen as the base for additional mesh sensitivity studies.

Table A4
Results of the mesh sensitivity analysis for thermo-mechanical simulations.

	Units	MPa						/
	Parameter	σ_{max}						Num. of FE
		Monoblock	Cu caging	Pipe	Cu interlayer	Support	Connection weld	
1	extra coarse	271.45	400.76	182.42	156.78	126.16	128.53	64,907
2	coarse	283.71	313.00	223.41	154.53	136.98	131.26	92,314
3	medium	293.63	347.15	201.01	155.19	146.07	131.08	345,509
4	fine	324.08	391.35	241.67	149.75	145.87	141.37	677,796
5	finer	351.36	413.71	264.60	149.93	147.58	145.56	1,505,875

(*continued on next page*)

Table A4 (*continued*)

	Units	MPa						/
	Parameter	σ_{max}						Num. of FE
		Monoblock	Cu caging	Pipe	Cu interlayer	Support	Connection weld	
6	extra fine	372.23	503.26	288.93	153.48	155.43	146.59	3,218,733
7	fine 2	315.94	391.33	233.04	173.37	145.8	141.41	728,498
8	fine 3	307.76	391.31	228.14	192.51	145.75	141.44	829,916

	Units	MPa						/
	Parameter	σ_{avg}						Num. of FE
		Monoblock	Cu caging	Pipe	Cu interlayer	Support	Connection weld	
1	extra coarse	60.36	39.80	65.14	71.23	26.72	68.21	64,907
2	coarse	52.30	32.91	60.78	70.98	25.45	69.14	92,314
3	medium	50.00	30.72	59.55	70.93	25.24	69.05	345,509
4	fine	50.03	29.67	58.85	71.64	24.95	69.53	677,796
5	finer	51.79	29.25	58.52	71.21	25.02	69.48	1,505,875
6	extra fine	50.5	28.8	58.59	71.16	25.07	69.39	3,218,733
7	fine 2	49.91	29.68	58.85	71.4	24.94	69.57	728,498
8	fine 3	49.81	29.68	58.86	71.37	24.94	69.59	829,916

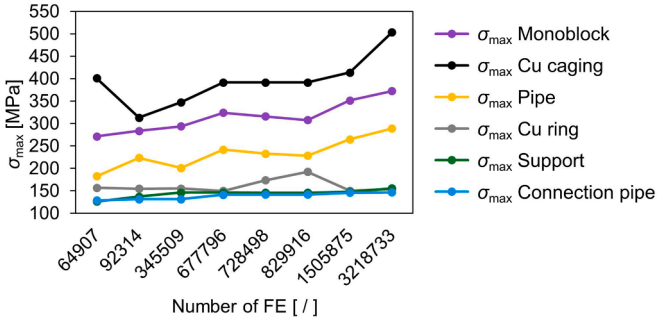

Fig. A3. Mesh sensitivity convergence for thermo-mechanical simulations.

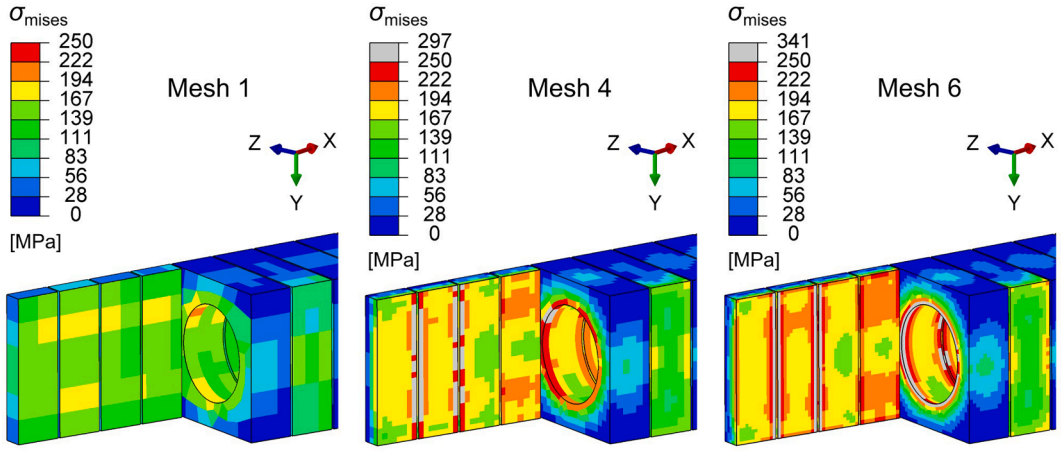

Fig. A4. Mesh sensitivity comparison between meshes of monoblocks for thermo-mechanical simulations.

Two additional meshes 7 and 8 were created, where the only difference is the number of FE through thickness in the Cu interlayer, which changed from 1 to 2 to 4 in meshes 4, 7 and 8, respectively. The resulting Mises stress distribution is shown in Fig. A5, which depicts the stress concentration on the edge of the Cu interlayer and, increasing stresses with higher number of FE. Based on these results, it was therefore concluded that mesh 7 is sufficient for further simulations (Fig. A6), since it properly describes the stresses with a lower number of FE as compared to mesh 8. Because these simulations were tested with linear-elastic material properties, three additional simulations were performed using meshes 4, 7 and 8 and ideal plasticity behavior of copper material, since the yield strength was exceeded. As it could be expected, the stresses at the yield value were obtained, but the maximum equivalent plastic strain was growing in a similar fashion as did the Mises stresses with increasing number of FE in the Cu interlayer thickness. This final test confirms mesh 7 to be used in the final PFU simulations.

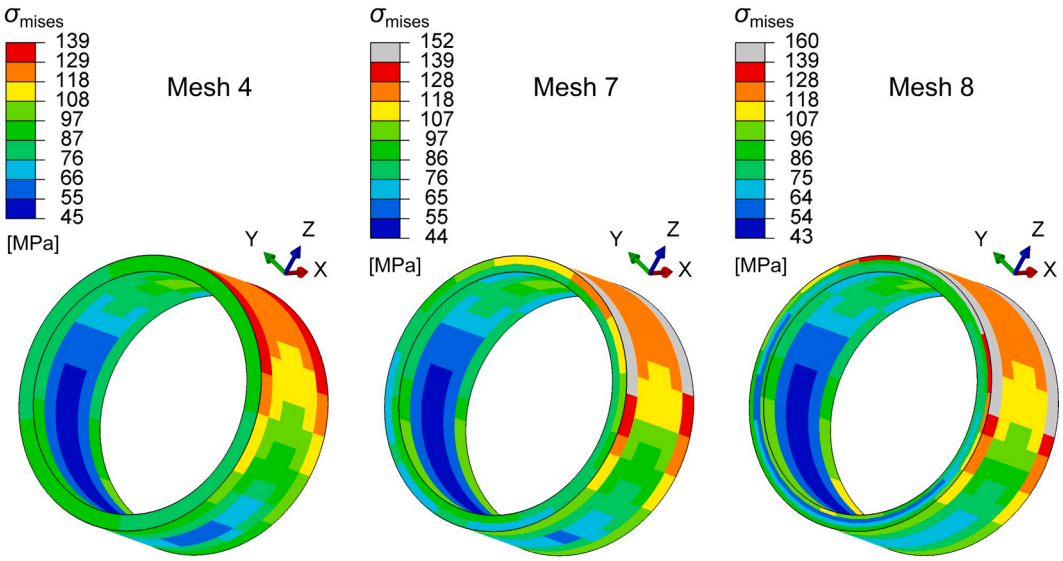

Fig. A5. Mesh sensitivity comparison between meshes of Cu interlayer for thermo-mechanical simulations

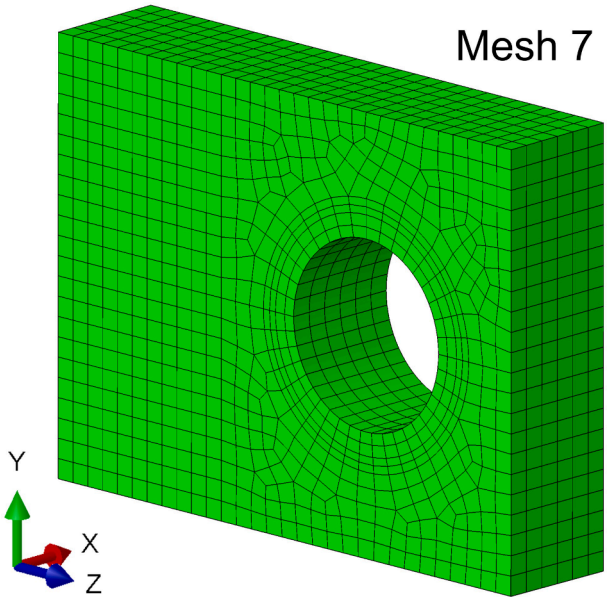

Fig. A6. Chosen mesh for thermo-mechanical simulations

Appendix B. Heat flux load projection on the pipes

The heat flux distributions on the PFU components were obtained from plasma simulations [17]. The heat flux boundary condition for the CFD simulations is uniform in the toroidal direction on the top surfaces of the monoblocks. On the pipes, a projection of heat fluxes as depicted in Fig. B1 (left) was used assuming a cosine function with the maximum value at the top of the pipe wall and zero at the sides, as represented in Fig. B1 (right) with Eq. (B1) and Eq. (B2).

$$z'^2 + y'^2 = R^2 \rightarrow z' = \sqrt{R^2 - y'^2} \tag{B1}$$

$$\cos(\theta) = \frac{z'}{R} = \frac{\sqrt{R^2 - y'^2}}{R} \tag{B2}$$

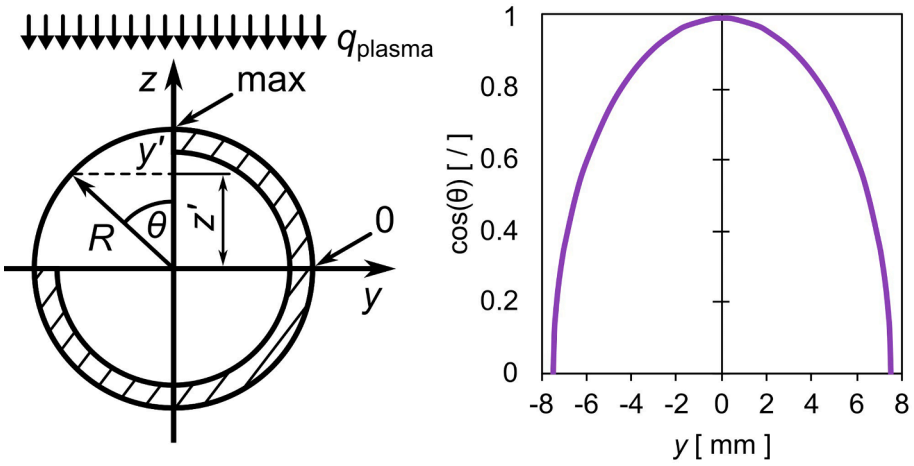

Fig. B1. Heat flux projection (left) and scaling function (right) on a pipe.

References

[1] R. Martone, R. Albanese, F. Crisanti, P. Martin, A. Pizzuto, DTT Divertor Tokamak Test facility – Interim Design Report, 2019. https://www.dtt-project.it/DTT_IDR_2019_WEB.pdf (accessed October 2, 2023).

[2] F. Crisanti, R. Albanese, G. Granucci, R. Martone, P. Sonato, The Divertor Tokamak Test facility proposal: Physical requirements and reference design, Nucl. Mater. Energy 12 (2017) 1330–1335, https://doi.org/10.1016/j.nme.2017.05.008.

[3] E. Visca, S. Roccella, P. Rossi, D. Candura, M. Palermo, Fabrication and acceptance of ITER vertical target divertor full scale plasma facing units fabricated by HRP, Fusion Eng. Des. 124 (2017) 191–195, https://doi.org/10.1016/j.fusengdes.2017.03.012.

[4] A. Durif, M. Richou, J.-M. Bergheau, L. Gallais, G. Kermouche, G. Pintsuk, T-REX: Numerical tool for tungsten damage assessment for DEMO, J. Nucl. Mater. 569 (2022) 153906, https://doi.org/10.1016/j.jnucmat.2022.153906.

[5] Y. Corre, M.-H. Aumeunier, A. Durif, J. Gaspar, K. Krieger, T. Loewenhoff, M. Richou, S. Ratynskaia, Q. Tichit, Y. Anquetin, R. Dejarnac, M. Diez, L. Dubus, M. Firdaouss, J. Gerardin, A. Grosjean, J.P. Gunn, T. Loarer, P. Maget, C. Martin, K. Paschalidis, E. Tsitrone, M. Wirtz, Testing of ITER-grade plasma facing units in the WEST tokamak: Progress in understanding heat loading and damage mechanisms, Nucl. Mater. Energy 37 (2023) 101546, https://doi.org/10.1016/j.nme.2023.101546.

[6] V. Menon, D. Krishnan, J. Parmar, S. Trapasya, S. Khirwadkar, Thermo-structural analysis of ITER divertor for normal operating conditions, Fusion Eng. Des. 180 (2022) 113152, https://doi.org/10.1016/j.fusengdes.2022.113152.

[7] E. Visca, S. Roccella, D. Candura, M. Palermo, P. Rossi, A. Pizzuto, G.P. Sanguinetti, A. Mancini, L. Verdini, E. Cacciotti, V. Cerri, G. Mugnaini, A. Reale, G. Giacomi, HRP facility for fabrication of ITER vertical target divertor full scale plasma facing units, Fusion Eng. Des. 98–99 (2015) 1407–1410, https://doi.org/10.1016/j.fusengdes.2014.12.010.

[8] J.-H. You, H. Greuner, B. Böswirth, K. Hunger, S. Roccella, H. Roche, High-heat-flux performance limit of tungsten monoblock targets: Impact on the armor materials and implications for power exhaust capacity, Nucl. Mater. Energy 33 (2022) 101307, https://doi.org/10.1016/j.nme.2022.101307.

[9] J.H. You, E. Visca, T. Barrett, B. Böswirth, F. Crescenzi, F. Domptail, G. Dose, M. Fursdon, F. Gallay, H. Greuner, K. Hunger, A. Lukenskas, A.v. Müller, M. Richou, S. Roccella, C. Vorpahl, K. Zhang, High-heat-flux technologies for the European demo divertor targets: State-of-the-art and a review of the latest testing campaign, J. Nucl. Mater. 544 (2021) 152670, https://doi.org/10.1016/j.jnucmat.2020.152670.

[10] S. Roccella, G. Dose, T. Barrett, E. Cacciotti, L. Dupont, F. Gallay, H. Greuner, M. Richou, A. Tatì, E. Visca, J.-H. You, Ultrasonic test results before and after high heat flux testing on W-monoblock mock-ups of EU-DEMO vertical target, Fusion Eng. Design 160 (2020) 111886, https://doi.org/10.1016/j.fusengdes.2020.111886.

[11] J.H. You, E. Visca, T. Barrett, B. Böswirth, F. Crescenzi, F. Domptail, M. Fursdon, F. Gallay, B.-E. Ghidersa, H. Greuner, M. Li, A.v. Müller, J. Reiser, M. Richou, S. Roccella, Ch. Vorpahl, European divertor target concepts for DEMO: Design rationales and high heat flux performance, Nucl. Mater. Energy 16 (2018) 1–11, https://doi.org/10.1016/j.nme.2018.05.012.

[12] M. Li, J.-H. You, Structural impact of creep in tungsten monoblock divertor target at 20 MW/m2, Nucl. Mater. Energy 14 (2018) 1–7, https://doi.org/10.1016/j.nme.2017.12.001.

[13] J. Du, Y. Yuan, M. Wirtz, J. Linke, W. Liu, H. Greuner, FEM study of recrystallized tungsten under ELM-like heat loads, J. Nucl. Mater. 463 (2015) 219–222, https://doi.org/10.1016/j.jnucmat.2014.10.044.

[14] S. Garitta, T. Batal, A. Durif, M. Firdaouss, M. Missirlian, H. Roche, P. Testoni, V. Tomarchio, M. Richou, Thermal and structural analysis of JT-60SA actively cooled divertor target submitted to high heat flux, Fusion Eng. Des. 199 (2024) 114133, https://doi.org/10.1016/j.fusengdes.2023.114133.

[15] M. Angelucci, Report on Hydraulic analysis of the divertor module 2021: Deliverable DIV-IDTT.S.02-T003-D001, (2021). https://idm.euro-fusion.org/default.aspx?uid=2PHN6J (accessed October 10, 2023).

[16] G. Dose, F. Giorgetti, S. Roccella, Design of a standard divertor module: Deliverable DIV-IDTT.S.01-T001-D003, (2021). https://idm.euro-fusion.org/default.aspx?uid=2PHLBP (accessed October 10, 2023).

[17] P. Innocente, R. Ambrosino, S. Brezinsek, G. Calabrò, A. Castaldo, F. Crisanti, G. Dose, R. Neu, S. Roccella, Design of a multi-configurations divertor for the DTT facility, Nucl. Mater. Energy 33 (2022) 101276, https://doi.org/10.1016/j.nme.2022.101276.

[18] P. Tarfila, B. Končar, O.C. Garrido, G. Dose, F. Giorgetti, S. Roccella, Development of a thermohydraulic model For DTT PFU, in: Nuclear Society of Slovenia, 2022: p. 1012.1.-1012.8. https://www.djs.si/nene2022/proceedings/htm/pdf/NENE2022_1012.pdf (accessed October 2, 2023).

[19] B. Končar, P. Tarfila, O.C. Garrido, PFU integrated thermohydraulic and thermomechanical model: Deliverable DIV-IDTT.S.01b-T001-D004, (2022). https://idm.euro-fusion.org/default.aspx?uid=2QA9YT (accessed October 10, 2023).

[20] Structural Design Criteria for ITER In-vessel Components (SDC-IC), (2012).

[21] ANSYS Workbench, (2022). https://www.ansys.com/products/ansys-workbench (accessed January 9, 2024).

[22] Abaqus FEA, (2022). https://www.3ds.com/products/simulia/abaqus (accessed January 9, 2024).

[23] Structural Design Criteria for ITER In-vessel Components (SDC-IC) - Appendix_A, Materials Design Limit Data, (2013).

[24] ANSYS CFX, (2022). https://www.ansys.com/products/fluids/ansys-cfx (accessed January 9, 2024).

[25] H. Bufferand, G. Ciraolo, Y. Marandet, J. Bucalossi, P. Ghendrih, J. Gunn, N. Mellet, P. Tamain, R. Leybros, N. Fedorczak, F. Schwander, E. Serre, Numerical modelling for divertor design of the WEST device with a focus on plasma–wall interactions, Nucl. Fusion 55 (2015) 053025, https://doi.org/10.1088/0029-5515/55/5/053025.

[26] P. Liu, X. Qian, X. Mao, W. Song, X. Peng, Study on creep-fatigue of heat sink in W/CuCrZr divertor target based on a new approach to creep life, Nucl. Mater. Energy 25 (2020) 100846, https://doi.org/10.1016/j.nme.2020.100846.

[27] M. Fursdon, J.-H. You, M. Li, Towards reliable design-by-analysis for divertor plasma facing components – Guidelines for inelastic assessment (part 1: Unirradiated), Fusion Eng. Des. 147 (2019) 111234, https://doi.org/10.1016/j.fusengdes.2019.06.007.

[28] ASME - Boiler and Pressure Vessel Code (BPVC), (n.d.). https://www.asme.org/codes-standards/bpvc-standards.